Available online at www.sciencedirect.com
ScienceDirect
Journal of Computational Physics 226 (2007) 2028–2043
JOURNAL OF COMPUTATIONAL PHYSICS
www.elsevier.com/locate/jcp

A LBM–DLM/FD method for 3D fluid–structure interactions

Xing Shi [a], Siak Piang Lim [b,*]

[a] Singapore-MIT Alliance, National University of Singapore, 4 Engineering Drive 3, Singapore 117576, Singapore
[b] Department of Mechanical Engineering, National University of Singapore, 10 Kent Ridge Crescent, Singapore 119260, Singapore

Received 29 September 2006; received in revised form 21 May 2007; accepted 26 June 2007
Available online 20 July 2007

Abstract

The previously developed LBM–DLM/FD method derived from the lattice Boltzmann method and the distributed Lagrange multiplier/fictitious domain method is extended to deal with 3D fluid–structure interactions. In our current algorithm, the fluid motion is solved by LBM, the deformation of the solid body is solved by the finite element method, and the Lagrange multiplier is solved on the low-order mesh. Three numerical examples are employed to validate the LBM–DLM/FD method and reveal the potential of the method to deal with the fluid/elastic-body interaction problems.

Keywords: Lattice Boltzmann method; Distributed Lagrange multiplier; Fictitious domain method; Fluid–structure interactions; Fluid/elastic-body interactions; High-order finite element method

1. Introduction

Fluid–structure interactions widely exist in various kinds of phenomena in nature and engineering. Particularly in the biomechanics field (e.g. blood flow in elastic vessels [1], aortic or heart valves [2], deformations and aggregations of the red blood cells and white blood cells [3], cell adhesion [4], cell trap and separation), the mechanism of fluid–structure interactions plays a key role. As an alterative method to laboratory experiments, numerical simulation attracts more and more interests of researchers. A variety of numerical methods for the fluid–structure systems have been developed from different backgrounds.

Generally, it is convenient for the flow field to be solved in the Eulerian frame where the mesh is fixed, whereas the Lagrangian description is more suitable for the solid deformation and motion. In the fluid–structure system, a straightforward strategy for the fluid–structure coupling is to directly treat the fluid–structure interface as a moving boundary of fluid mesh, as in the conventional ALE (arbitrary Lagrangian–Eulerian) method [5]. The accuracy of the fluid–structure interface presented on the fluid mesh is guaranteed, but the trade-off is mesh updating due to the moving interface and re-meshing due to the large deformation of the interface or the too distorted mesh. The re-meshing procedure is always time-consuming and difficult in

* Corresponding author.
E-mail addresses: mecshix@yahoo.com (X. Shi), mpelimsp@nus.edu.sg (S.P. Lim).

0021-9991/$ - see front matter
doi:10.1016/j.jcp.2007.06.031

complex topology. Moreover, when the solid deformation is large and the geometry is complex, the algorithm cannot keep robust [2].

Another algorithm of coupling the fluid and the structure is accomplished by proposing a pseudo body force like multiplier to constrain the fluid velocity and structure velocity. The fluid mesh is independent of the motion of solid mesh. The algorithms of distribution and interpolation are adopted to impose the fluid–structure coupling on each fluid or solid mesh. The re-meshing is not required. The original immersed boundary (IB) method of Peskin [6] was developed for the volumeless flexible solid body submerged in flow, and its capacity has been enhanced by other variants such as immersed finite element method (IFEM) [7]. The fictitious domain method (FDM) was firstly proposed for particulate flows [8,9], and then extended to fluid/elastic–structure interactions [10,11]. Both IFEM and FDM for flexible structures are more accurate and realistic than original IB because the solid problem is solved by finite element method rather than using fiber network presentation and volumelessness assumption in IB.

The lattice Boltzmann method (LBM) has been widely used in different areas of computational fluid dynamics (CFD) as an alternative choice to its continuum counterpart [12,13]. In the area of fluid–structure interactions, the bounce-back rule was first introduced to impose the fluid–structure coupling [14]. It was proved robust and efficient for particulate flows, especially in the case of large number of particles. The bounce-back rule was also applied to fluid/rigid–structure interactions [15], fluid–membrane interactions [16] and fluid/flexible–elastic-body interactions [17]. Later, the IB method was incorporated successfully into LBM for the 2D and 3D fluid–particle systems [18]. Recently, the LBM–DLM/FD method [19], which combines the ideas of the LBM and FDM, has been proposed for the two-dimensional fluid/elastic–structure interactions.

The aim of the present study is to extend the LBM–DLM/FD method from 2D to 3D. The new idea is the combination of LBM and FD method, which lets the proposed LBM–DLM/FD method inherit the advantages of both methods. Compared with IB based method, the LBM–DLM/FD method has the potential to deal with more general solid sub-problems. In the following sections, we first briefly describe the roots of the LBM–DLM/FD method: DLM/FD and LBM. Subsequently, we present the equations of LBM–DLM/FD for fluid–structure interactions. Finally, the method is applied to three numerical examples, a plate in a channel flow, the flow past two spheres placed side by side and a spherical shell in a duct flow to validate the algorithm and demonstrate the capability of the method.

2. Mathematical formulation

2.1. DLM/FD method

Before the presentation of our method, let us briefly introduce the fictitious domain method for fluid–elastic structure interaction. The FDM was initially designed for fluid/rigid-body system. In recent years, the fictitious domain/mortar element method [10] and the DLM/FD method [11] have been proposed for the fluid/elastic–structure interactions by considering the elastic-solid governing equations. We prefer the DLM/FD formulation for its greater generality. The basic idea of fictitious domain method is to fill the solid domain with fluid, which simplifies the fluid boundary geometry greatly. The distributed Lagrange multiplier (DLM) is introduced to impose the kinematical constraint in the solid domain, or the fictitious fluid domain. Let us use Ω_f and Ω_s to define the extended fluid and structure domain, respectively. The weak-form equations of DLM/FD method for the elastic structure immersed in a Newtonian fluid are expressed as [11]:

$$\int_{\Omega_f} \rho_f \left(\frac{\partial \mathbf{u}_f}{\partial t} + \mathbf{u}_f \cdot \nabla \mathbf{u}_f - \mathbf{f}_f \right) \cdot \boldsymbol{\varphi}_f \, d\Omega_f + \int_{\Omega_f} (-p\mathbf{I} + \eta(\nabla \mathbf{u}_f + (\nabla \mathbf{u}_f)^T)) : \nabla \boldsymbol{\varphi}_f \, d\Omega_f - \int_{\Omega_f} \boldsymbol{\lambda} \cdot \boldsymbol{\varphi}_f \, d\Omega_f = 0, \quad (1)$$

$$\int_{\Omega_f} \psi_f \nabla \cdot \mathbf{u}_f \, d\Omega_f = 0, \quad (2)$$

$$\int_{\Omega_s} \left((\rho_s - \rho_f) \frac{d\mathbf{u}_s}{dt} - (\rho_s \mathbf{f}_s - \rho_f \mathbf{f}_f) \right) : \boldsymbol{\varphi}_s \, d\Omega_s + \int_{\Omega_s} (\boldsymbol{\sigma}_s - \boldsymbol{\sigma}_f) : \nabla \boldsymbol{\varphi}_s \, d\Omega_s + \int_{\Omega_s} \boldsymbol{\lambda} \cdot \boldsymbol{\varphi}_s \, d\Omega_s = 0, \quad (3)$$

$$\int_{\Omega_s} (\mathbf{u}_s - \mathbf{u}_f) \cdot \boldsymbol{\gamma} \, d\Omega_s = 0, \tag{4}$$

where $\mathbf{u}$ is the velocity, ρ is the mass density, $\mathbf{f}$ is the body force and $\boldsymbol{\sigma}$ is the stress and the subscripts f and s are introduced to differentiate between the variables of the fluid and structure, respectively. p denotes the fluid pressure, η is the dynamic viscosity of the fluid. $\boldsymbol{\lambda}$ is the Lagrange multiplier. $\boldsymbol{\varphi}_f$, ψ_f, $\boldsymbol{\varphi}_s$ and $\boldsymbol{\gamma}$ are the corresponding weight functions for the fluid velocity, the fluid pressure, the solid displacement and the Lagrange multiplier, respectively. When the constitutive equations for solid are added, the above equations are closed.

The above equations can be solved by either the full coupling method or decoupling method. The full coupling method solves all variables at the same time [2]. The decoupling method [11] is a fractional step method that decomposes the entire system into several sub-systems. Although the decoupling method is expected to be less accurate than the full coupling method, it is simpler and much more efficient, and therefore is used in the present study.

2.2. Lattice Boltzmann method

Unlike the classic macroscopic fluid equations, lattice Boltzmann equation describes the fluid flow from the microscopic kinetics theory. In order to work with DLM, the discrete Lattice Boltzmann equations of single relaxation time model with external body force are required [12,13,20]:

$$f_i(t+\delta_t, \mathbf{x}+\mathbf{e}_i\delta_t) = f_i(t,\mathbf{x}) - \frac{1}{\tau}(f_i - f_i^{eq}) + \frac{\mathbf{f}_f \cdot (\mathbf{e}_i - \mathbf{u}_f)}{c_s^2} f_i^{eq}\delta_t, \tag{5}$$

where $f_i(t,\mathbf{x})$ is single-particle distribution function on the i-direction microscopic velocity $\mathbf{e}_i$, as shown in Fig. 1, $\mathbf{f}_f$ is the external force, τ is the relaxation time, associating with the kinetic viscosity of fluids, δ_t denotes the time step, $\Omega_i = -\frac{1}{\tau}(f_i - f_i^{eq})$ is called the collision operator, $\mathbf{u}_f$, ρ_f are the macroscopic velocity and mass density of the fluid, obtained from the distribution functions as follows [12]

$$\rho_f = \sum_i f_i, \quad \rho_f \mathbf{u}_f = \sum_i f_i \mathbf{e}_i. \tag{6}$$

For 3DQ15 model [21] shown in Fig. 1:

$$\begin{aligned}
&\mathbf{e}_0 = (0,0,0),\\
&\mathbf{e}_1 = (1,0,0)\frac{\delta_x}{\delta_t}, \quad \mathbf{e}_2 = (-1,0,0)\frac{\delta_x}{\delta_t}, \quad \mathbf{e}_3 = (0,1,0)\frac{\delta_x}{\delta_t},\\
&\mathbf{e}_4 = (0,-1,0)\frac{\delta_x}{\delta_t}, \quad \mathbf{e}_5 = (0,0,1)\frac{\delta_x}{\delta_t}, \quad \mathbf{e}_3 = (0,0,-1)\frac{\delta_x}{\delta_t},\\
&\mathbf{e}_7 = (1,1,1)\frac{\delta_x}{\delta_t}, \quad \mathbf{e}_8 = (-1,-1,-1)\frac{\delta_x}{\delta_t}, \quad \mathbf{e}_9 = (-1,1,1)\frac{\delta_x}{\delta_t}, \quad \mathbf{e}_{10} = (1,-1,-1)\frac{\delta_x}{\delta_t},\\
&\mathbf{e}_{11} = (-1,-1,1)\frac{\delta_x}{\delta_t}, \quad \mathbf{e}_{12} = (1,1,-1)\frac{\delta_x}{\delta_t}, \quad \mathbf{e}_{13} = (1,-1,1)\frac{\delta_x}{\delta_t}, \quad \mathbf{e}_{14} = (-1,1,-1)\frac{\delta_x}{\delta_t},
\end{aligned} \tag{7}$$

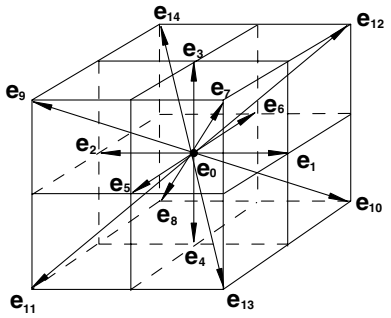

Fig. 1. D3Q15 model.

where δ_x is the lattice spacing. The corresponding equilibrium function can be chosen in the following form [12]:

$$f_i^{\mathrm{eq}} = w_i \rho_{\mathrm{f}} \left[1 + \frac{3}{c^2}(\mathbf{e}_i \cdot \mathbf{u}_{\mathrm{f}}) + \frac{9}{2c^4}(\mathbf{e}_i \cdot \mathbf{u}_{\mathrm{f}})^2 - \frac{3}{2c^2}\mathbf{u}_{\mathrm{f}}^2 \right], \tag{8}$$

$c = \delta_x/\delta_t$ and $c_{\mathrm{s}} = c/\sqrt{3}$ is called the sound speed. The weight factors of D3Q15 are:

$$\begin{aligned} w_0 &= \frac{2}{9}, \\ w_i &= \frac{1}{9}, \quad i = 1\text{–}6, \\ w_i &= \frac{1}{72}, \quad i = 7\text{–}14. \end{aligned} \tag{9}$$

With the help of the Chapman–Enskog procedure, the macroscopic mass and momentum equations can be recovered from the lattice Boltzmann equations [12,22]:

$$\frac{\partial \rho_{\mathrm{f}}}{\partial t} + \nabla \cdot (\rho_{\mathrm{f}} \mathbf{u}_{\mathrm{f}}) = 0, \tag{10}$$

$$\frac{\partial (\rho_{\mathrm{f}} \mathbf{u}_{\mathrm{f}})}{\partial t} + \nabla \cdot (\rho_{\mathrm{f}} \mathbf{u}_{\mathrm{f}} \mathbf{u}_{\mathrm{f}}) = \nabla \cdot (-c_{\mathrm{s}}^2 \rho_{\mathrm{f}} \mathbf{I} + \rho_{\mathrm{f}} \nu (\nabla \mathbf{u}_{\mathrm{f}} + \nabla \mathbf{u}_{\mathrm{f}}^{\mathrm{T}})) + \rho_{\mathrm{f}} \mathbf{f}_{\mathrm{f}}. \tag{11}$$

In the D3Q15 models, the kinematic viscosity is $\nu = \frac{1}{6}(2\tau - 1)\frac{\delta_x^2}{\delta_t}$. If $f_i = f_i^{\mathrm{eq}} + \varepsilon f_i^1 + \varepsilon^2 f_i^2 + \mathrm{O}(\varepsilon^3)$, the fluid stress tensor is [12]

$$\boldsymbol{\sigma}_{\mathrm{f}} = -c_{\mathrm{s}}^2 \rho_{\mathrm{f}} \mathbf{I} - \left(1 - \frac{1}{2\tau}\right) \sum_i f_i^1 \mathbf{e}_i \mathbf{e}_i, \tag{12}$$

where ε is the small parameter in Chapman–Enskog procedure. In the limit case of incompressible fluid, which requires $|\mathbf{u}_{\mathrm{f}}| \ll |\mathbf{e}_i|$, the evolution equation (Eq. (5)) is simplified to:

$$f_i(t + \delta_t, \mathbf{x} + \mathbf{e}_i \delta_t) = f_i(t, \mathbf{x}) - \frac{1}{\tau}(f_i - f_i^{\mathrm{eq}}) + \frac{w_i \delta_t \rho_{\mathrm{f}}}{c_{\mathrm{s}}^2}(\mathbf{f}_{\mathrm{f}} \cdot \mathbf{e}_i). \tag{13}$$

2.3. LBM–DLM/FD method

Compared with the Navier–Stokes equations, there are no nonlinear convection terms in the lattice Boltzmann equations. Every lattice has relations only with its neighborhoods at each time step, which facilitates parallel coding. The pressure is directly obtained. So we decide to replace the macroscopic fluid equations by the lattice Boltzmann equations. The role of the Lagrange multiplier is not only the constraint for the velocity but also can be regarded as a pseudo body force, which makes it possible to substitute $\boldsymbol{\lambda}$ to $\rho_{\mathrm{f}} \mathbf{f}_{\mathrm{f}}$ in the LBEs. That yields our LBM–DLM/FD equations:

$$f_i(t + \delta_t, \mathbf{x} + \mathbf{e}_i \delta_t) = f_i(t, \mathbf{x}) - \frac{1}{\tau}(f_i - f_i^{\mathrm{eq}}) + \frac{w_i \delta_t}{c_{\mathrm{s}}^2}(\boldsymbol{\lambda} \cdot \mathbf{e}_i), \tag{14}$$

$$\int_{\Omega_{\mathrm{s}}} \left((\rho_{\mathrm{s}} - \rho_{\mathrm{f}}) \frac{\mathrm{d}\mathbf{u}_{\mathrm{s}}}{\mathrm{d}t} - (\rho_{\mathrm{s}} \mathbf{f}_{\mathrm{s}} - \rho_{\mathrm{f}} \mathbf{f}_{\mathrm{f}}) \right) : \boldsymbol{\varphi}_{\mathrm{s}} \, \mathrm{d}\Omega_{\mathrm{s}} + \int_{\Omega_{\mathrm{s}}} (\boldsymbol{\sigma}_{\mathrm{s}} - \boldsymbol{\sigma}_{\mathrm{f}}) : \nabla \boldsymbol{\varphi}_{\mathrm{s}} \, \mathrm{d}\Omega_{\mathrm{s}} + \int_{\Omega_{\mathrm{s}}} \boldsymbol{\lambda} \cdot \boldsymbol{\varphi}_{\mathrm{s}} \, \mathrm{d}\Omega_{\mathrm{s}} = 0, \tag{15}$$

$$\int_{\Omega_{\mathrm{s}}} (\mathbf{u}_{\mathrm{s}} - \mathbf{u}_{\mathrm{f}}) \cdot \boldsymbol{\gamma} \, \mathrm{d}\Omega_{\mathrm{s}} = 0. \tag{16}$$

We decouple the entire system into the fluid and solid sub-problems with the fractional step scheme in the same manner as in the DLM/FD [11]. The present fractional step scheme is the following:

(1) Assuming that f_i^n, $\boldsymbol{\lambda}^n$ at the time step n is given, calculate f_i^* from Eq. (5) without the collision operator and then ρ_{f}^* and $\mathbf{u}_{\mathrm{f}}^*$ from Eq. (6). Here, the superscript "*" denotes an intermediate fractional step.

(2) Based on Eq. (15) and the solid constitutive equations, find the solid displacement $\mathbf{d}_s^{n+1}$ with the finite element method. The nonlinear equations are solved by the Newon–Raphson iterative method.
(3) Using the first-order accurate scheme, calculate the solid velocity from $\mathbf{u}_s^{n+1} = \frac{\mathbf{d}_s^{n+1} - \mathbf{d}_s^n}{\delta_t}$. Together with the velocity constraint (16) and the idea of the fractional time scheme, compute $\boldsymbol{\lambda}^{n+1}$ from the following equation:

$$\int_{\Omega_s} \boldsymbol{\lambda}^{n+1} \cdot \boldsymbol{\varphi}_s \, d\Omega_s = \int_{\Omega_s} \boldsymbol{\lambda}^n \cdot \boldsymbol{\varphi}_s \, d\Omega_s + \int_{\Omega_s} \rho_f^* \left(\frac{\mathbf{u}_s^{n+1} - \mathbf{u}_f^*}{\delta_t} \right) \cdot \boldsymbol{\varphi}_s \, d\Omega_s. \tag{17}$$

(4) Calculate the intermediate distribution function f_i^{**} from:

$$f_i^{**} = f_i^* + \frac{w_i \delta_t}{c_s^2} \left[(\boldsymbol{\lambda}_f^{n+1} - \boldsymbol{\lambda}_f^n) \cdot \mathbf{e}_i \right]. \tag{18}$$

(5) Calculate the distribution function f_i^{n+1} at the time step $n+1$ from:

$$f_i^{n+1} = f_i^{**} - \frac{1}{\tau}(f_i^{**} - f_i^{eq**}). \tag{19}$$

3. Applications

3.1. Plate in a flow between two planes

As shown in Fig. 2, a plate is placed in a pressure-driven flow between the top and bottom planes with the distance L. The plate is located symmetrically about the spanwise center plane. The wall boundary condition is enforced on the top and bottom planes, and the periodic boundary condition is imposed in the spanwise direction.

First, we will examine the Lagrange multiplier for its role in the fluid and solid interactions. In this test, the plate is considered rigid and fixed so that only the LBE and the Lagrange multiplier updating equations are taken into account. Two mesh systems, listed in Table 1, are utilized for comparison. The Reynolds number is defined as $Re = \frac{L^3 G}{8\nu^2}$ where G is the magnitude of pressure gradient, and is same for the two cases. The fluid mass density and the streamwise gradient are 1.0 and 6.0×10^{-4}, respectively.

Under the flow condition in this example, the force exerted on the plate by the fluid can be calculated in a straightforward manner from Lagrange multiplier without using the stress on the interface:

$$\mathbf{F}_s = -\int_{\Omega_s} \boldsymbol{\lambda} \, d\Omega_s. \tag{20}$$

The results from the classic LBM, where the bounce-back rule is applied on the plate to ensure the no-slip boundary, are utilized as the benchmark. In the bounce-back rule for a stationary wall, if a boundary exists

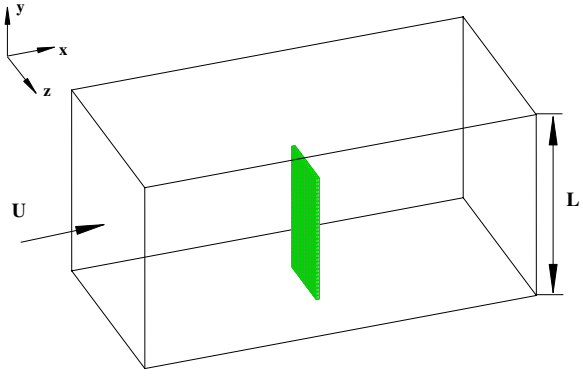

Fig. 2. A plate in a channel flow.

Table 1
The mesh systems

	Fluid		Lagrange multiplier	
	Mesh number	Domain size	Mesh number	Domain size
Mesh 1	$160 \times 30 \times 30$	$160 \times 30 \times 30$	$1 \times 10 \times 20$	$1 \times 10 \times 20$
Mesh 2	$320 \times 60 \times 60$	$320 \times 60 \times 60$	$1 \times 20 \times 40$	$1 \times 20 \times 40$

between $\mathbf{x}$ and $\mathbf{x} + \mathbf{e}_i\,\delta_t$, i is called a boundary link. The distribution function in the reflected direction i' is obtained as:

$$f_{i'}(t + \delta_t, \mathbf{x}) = f_i(t^+, \mathbf{x}), \tag{21}$$

where t^+ means post-collision. Due to the increment of momentum, the impulsive force exerted on the boundary along the link reads [23]:

$$\mathbf{F}_p\left(t, \mathbf{x} + \frac{1}{2}\mathbf{e}_i\delta_t\right) = \frac{2f_i(t^+, \mathbf{x})}{\delta t}\mathbf{e}_i. \tag{22}$$

The total force on the plate is the summation of the force along all boundary links:

$$\mathbf{F}_s = \sum \mathbf{F}_p\left(t + \mathbf{x} + \frac{1}{2}\mathbf{e}_i\delta_t\right). \tag{23}$$

The errors in velocity and pressure at the final steady state listed in Table 2 are defined as following:

$$E_v = \frac{\sqrt{\sum_{\text{all nodes}}(\mathbf{u}_{\text{DLM}} - \mathbf{u}_{\text{BK}}) \cdot (\mathbf{u}_{\text{DLM}} - \mathbf{u}_{\text{BK}})}}{\sqrt{\sum_{\text{all nodes}}\mathbf{u}_{\text{BK}} \cdot \mathbf{u}_{\text{BK}}}}, \quad E_p = \frac{\sqrt{\sum_{\text{all nodes}}(p_{\text{DLM}} - p_{\text{BK}})^2}}{\sqrt{\sum_{\text{all nodes}}p_{\text{BK}}^2}}. \tag{24}$$

The force derived from bounce-back rule is used to scale the hydrodynamic force in streamwise direction, i.e. $F_x^* = F_{\text{DLM}x}/F_{\text{BK}x}$. The subscripts 'DLM' and 'BK' denote the distributed Lagrange method and the bounce-back rule, respectively.

Table 2 shows that the results of LBM–DLM are close to the classic LBM with bounce-back rule, particularly in the case of fine mesh. To demonstrate more details, velocity contours in two characteristic planes in the streamwise direction from two methods with Mesh2 are compared in Fig. 3. One characteristic plane is the middle plane vertical to z-axis, called MXY, and the other is the middle plane vertical to y-axis, called MXZ.

We can find in Fig. 3 that the flow field solved using LBM–DLM is very close to that using LBM with bounce-back rule except some areas in the vicinity of the plate. Table 2 and Fig. 3 indicate that the Lagrange multiplier properly imposes the fluid–structure coupling, which gives the correct flow field and hydrodynamic force on the structure.

Then we consider the elastic deformation of the plate. To describe the constitutive relationship of solid structure, let $\mathbf{X}$ be the undeformed configuration of solid and $\mathbf{x}$ be the deformed current configuration. The deformation gradient is given by:

$$\mathbf{F} = \frac{\partial \mathbf{x}}{\partial \mathbf{X}} \tag{25}$$

and the related right Cauchy–Green tensor is $\mathbf{C} = \mathbf{F}^{\mathrm{T}}\mathbf{F}$. The solid adopted here is the neo-Hookean material defined by the strain energy density per unit [24,25] :

Table 2
Results in two mesh systems

	E_v	E_p	F_x^*
Mesh 1	0.0305	0.004412	1.201
Mesh 2	0.0143	0.000317	1.053

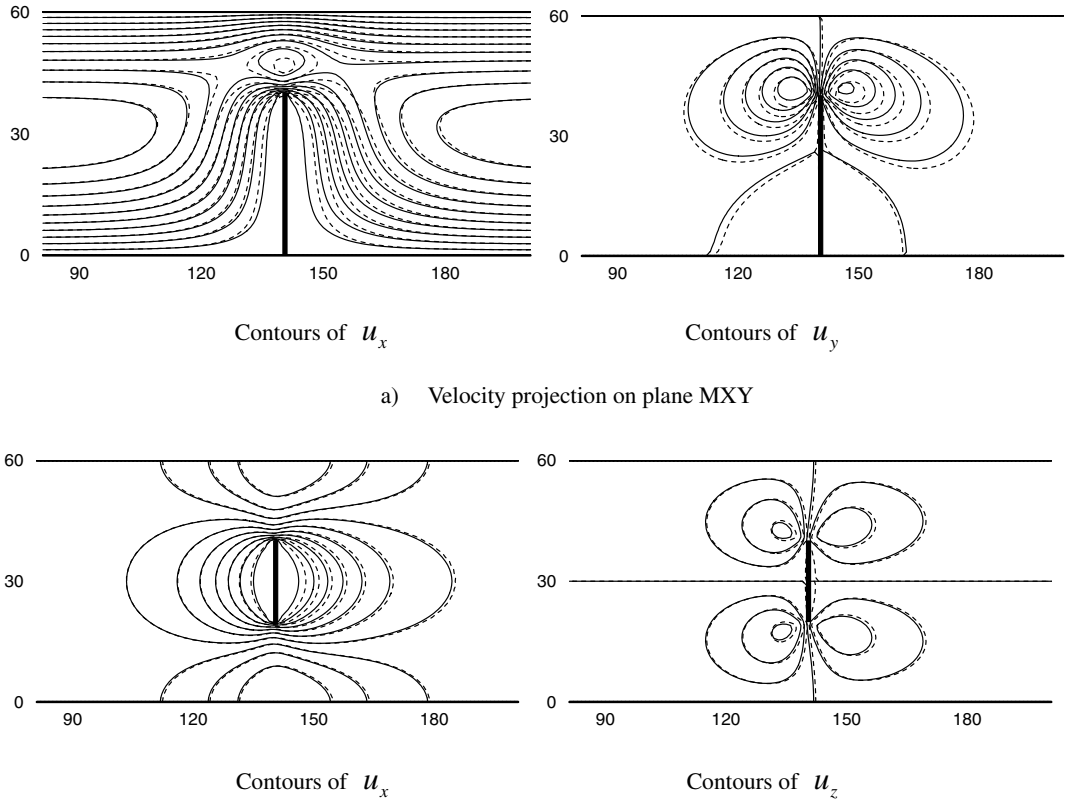

Fig. 3. Comparisons of two methods. The solid lines denote LBM–DLM and the dash lines denote LBM with bounce-back rule (Mesh2).

$$W(\mathbf{C}) = \frac{\mu}{2}(\mathrm{tr}(\mathbf{C}) - 3) - \mu \log J + \frac{\lambda}{2}(\log J)^2, \tag{26}$$

where $J = \det(\mathbf{F})$. The corresponding second Piola–Kirchhoff stress tensor can be derived as:

$$\mathbf{S} = 2\frac{\partial W}{\partial \mathbf{C}} = \mu(\mathbf{I} - \mathbf{C}^{-1}) + \lambda \log J \mathbf{C}^{-1} \tag{27}$$

and the Cauchy stress is presented as:

$$\boldsymbol{\sigma} = J^{-1}\mathbf{F} \cdot \mathbf{S} \cdot \mathbf{F}^{\mathrm{T}}. \tag{28}$$

In the present example, the size of fluid domain is $160 \times 30 \times 30$ and the size of the plate is $0.5 \times 20 \times 10$ with respect to the x–y–z directions. The plate is discretized into 72 27-node elements and placed 70 away from the inlet of the channel. One of the plate end is fixed on the bottom wall of the channel at $y = 0$. The relaxation time and the fluid mass density are given as 0.95 and 1.0, respectively. The oscillatory streamwise pressure gradient is:

$$\frac{\mathrm{d}p}{\mathrm{d}x} = P_0 \sin\left(\frac{2\pi}{T}t\right), \tag{29}$$

where P_0 is the amplification, being 1.5×10^{-4}, t is the time and T is the period. The solid has same mass density as the fluid and the material parameters are $\mu = 100$ and $\lambda = 1.0 \times 10^4$. The flow and the plate start from stationary state with all the velocities being zero.

Fig. 4 shows the streamlines over the deformed plate and the velocity projections on the MXY plane at different times. The plate swings due to the oscillation of the flow. At the initial stage, the fluid bends the plate

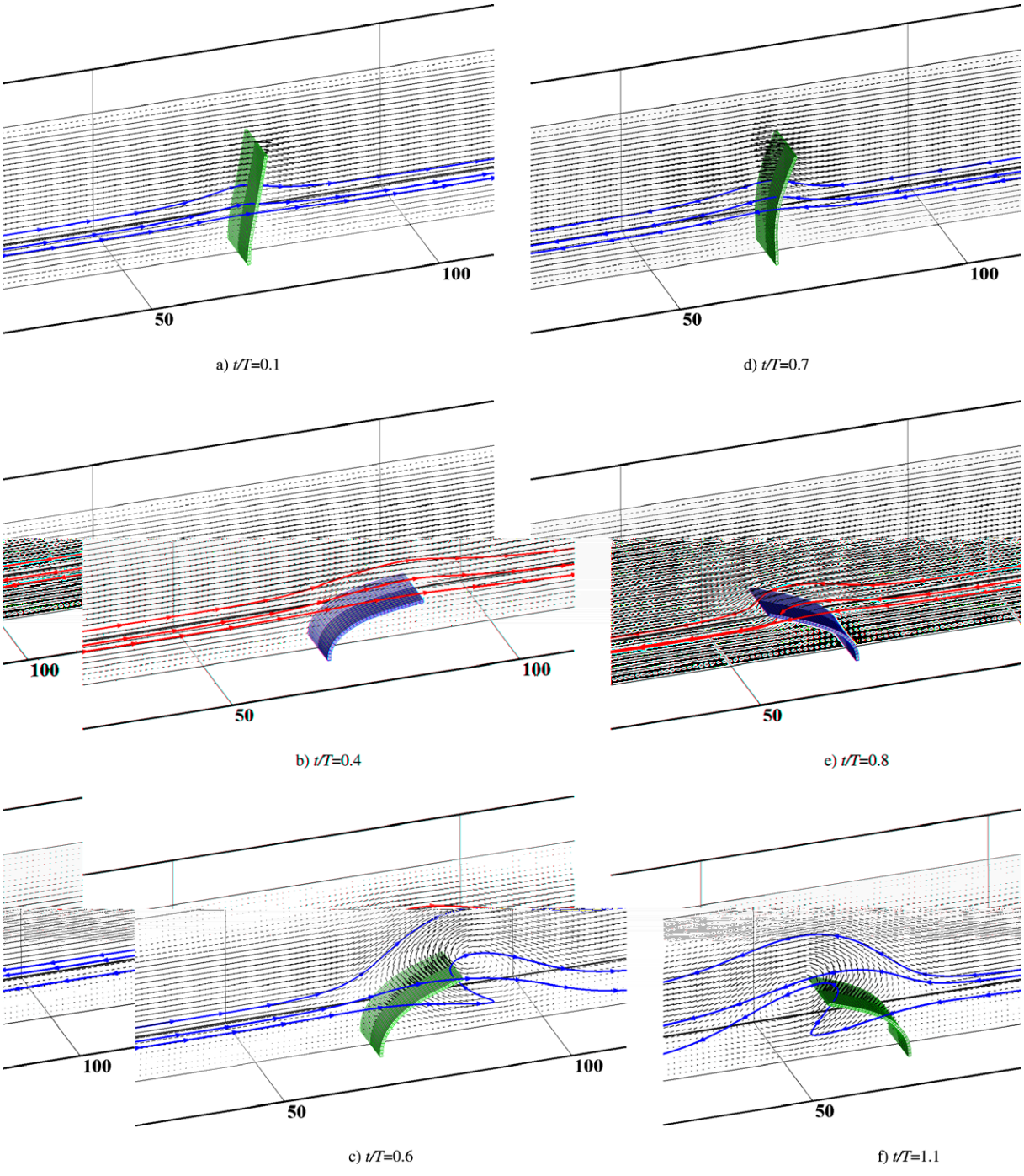

Fig. 4. Stream lines past the plate.

to the flow direction. As the flux increases, the deformation of plate becomes large, as shown in (a) and (b). In the second stage, when the pressure decreases, the flux decreases accordingly, and the hydrodynamic force on the plate cannot balance the inner elastic force in the significantly deformed plate, thus the plate bounces back. At this stage, the direction of the plate velocity is opposite to that of the main flow, resulting in a dramatic relative motion of the plate with respect to the fluid. We can find, in (c), a circulation region appears at the right-hand side of the plate. The swirl streamlines indicate that the more complex flow pattern is formed. Then

the flow direction reverses, and the plate motion is in phase with the flow again. The similar plate deformations and flow patterns to those in the previous two stages are exhibited in the reversed direction, as illustrated in (d)–(f).

In this numerical example, we also find the same restriction to the mesh size of Lagrange multiplier as in [11] in 2D cases: the range of the Lagrange multiplier mesh size is about one to two times of the fluid mesh size. Too fine Lagrange multiplier mesh would bring unphysical oscillation to the solution.

3.2. Flow past two spheres placed side by side

In this section, we discuss the proposed algorithm for the flow in complex geometry domains. The flow past two identical rigid spheres is employed as an example. As shown in Fig. 5, two spheres with the diameter D are placed side by side in a uniform flow. The flow direction is parallel to x axis and vertical to the line connecting the sphere centers. h denotes the distance between the sphere centers. For convenience, the x–z plane containing the sphere centers is called MXZ plane and the x–y plane at the midway of two sphere centers is called MXY plane. In current computation, the resolution of the sphere diameter is 28. Each sphere is divided into 10,293 tetrahedral elements with 2073 nodes. The undisturbed velocity U is set to 0.1 The Reynolds number is based on the sphere diameter:

$$Re = \frac{UD}{v}, \tag{30}$$

where v is the kinematic viscosity.

We first investigate the flow at $Re = 100$ with the two spheres separated by $h = 1.5D$. The size of the computation domain is $456 \times 260 \times 250$. The inlet is 156 ahead from the sphere center. When $Re < 200$, the flow reaches a steady status. Fig. 6 shows the distribution of streamwise velocity and the streamline on MXZ plane.

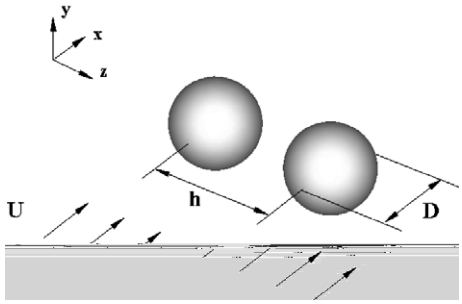

Fig. 5. Flow configuration.

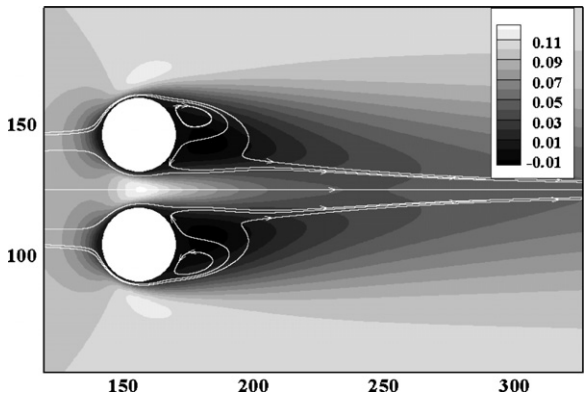

Fig. 6. Streamwise velocity distribution and streamlines on MXZ plane at $Re = 100$ for $h = 1.5D$.

In current configuration, the fluid flowing through the gap between the two spheres is accelerated, as indicated in Fig. 6, the maximum value of streamwise velocity appears in the gap. That is so-called 'nozzle effect'. The nozzle effect increases the local Reynolds number and changes the shape of the wake. Fig. 6 also shows that the wake behind each sphere is no longer axisymmetric in contrast with the wake of a single sphere. In order to demonstrate the weak region more clearly, the 3D pathlines or streamlines are plotted in Fig. 7. We define the local coordinates as the global coordinates translated to the center of the sphere with larger z value. Line A is the pathline of the fluid particle starting from the circulating region in the weak at $(19.0, 0.2, 1.0)$ in the local coordinate. The fluid particle swirls in the circulating region and approaches to the MXY plane, then exits the circulating region and goes downstream. Lines B and C exhibit the pathlines identified by the initial positions of the fluid particles at $(0.0, 15.0, 0.0)$ and $(0.0, 1.0, 15.0)$, respectively. Both lines perform the **S**-shape patterns without loop in the weak. Although the flow is not axisymmetric, it is still plane symmetric with respect to MXY and MXZ planes. These phenomena match that in [26].

The quantitative comparisons on the pressure coefficient, the drag coefficient and the lift coefficient are given in Fig. 8 and Table 3. The pressure coefficient is evaluated by:

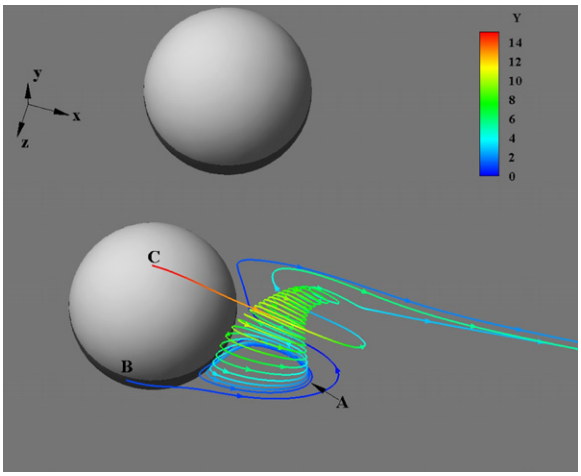

Fig. 7. 3D pathlines in the weak at $Re = 100$ for $h = 1.5D$.

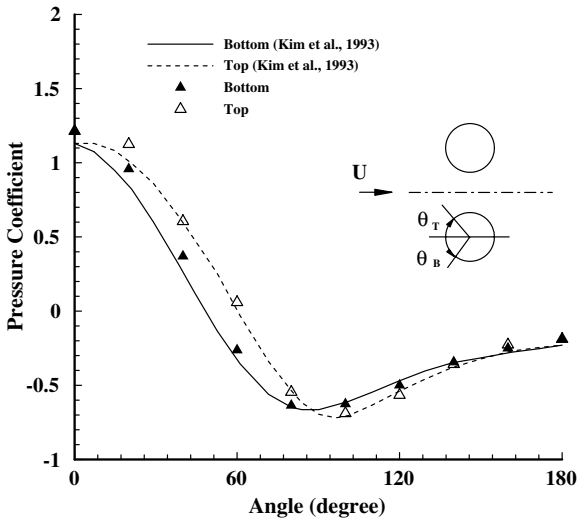

Fig. 8. Pressure coefficient distribution on the sphere surface in the MXZ plane at $Re = 100$ for $h = 1.5D$.

Table 3
Comparison on the drag coefficient and lift coefficient at $Re = 100$ for $h = 1.5D$

	C_d	C_{d0}	C_l
Kim et al. [26]	1.215	1.105	0.0783
Tsuji et al. [27]	1.289	1.18	–
Present	1.288	1.188	0.0928

C_{d0} is the drag coefficient for a single non-interactive sphere.

$$C_p = \frac{2(p - p_\infty)}{\rho_f U^2}, \tag{31}$$

where p_∞ is the undisturbed pressure. The drag coefficient is defined as:

$$C_d = \frac{8F_x}{\rho_f U^2 \pi D^2}. \tag{32}$$

And the lift coefficient:

$$C_l = \frac{8F_l}{\rho_f U^2 \pi D^2}, \tag{33}$$

where F_x and F_l are the components of force acting on the sphere in streamwise and lateral directions separately.

Fig. 8 reveals that the pressure distribution is not symmetric between the top and bottom surface, which leads to a contribution to the repelling lift force found in our computation. The increase of local Reynolds number due to the nozzle effect causes local shear rate rising. In Table 3, the drag is increased compared to the drag of a single non-interactive sphere.

Then we will observe vortices shedding behind the two spheres at $Re = 300$. The size of the computation domain is $480 \times 260 \times 250$. The inlet is 160 ahead from the sphere center. For a single sphere in a uniform flow, when the Reynolds number reaches around 280 and below 360, the plane symmetric hairpin shaped vortices are shed periodically behind the sphere. The orientation of the symmetric plane is arbitrary [29].

The vortical structure in the flow with the separation of $h = 1.5D$ is visualized by the method proposed by Jeong and Hussain [28] in Fig. 9. This distance is a strong coupled length for the spheres. It is found that the wake of each sphere is still plane symmetric, but the directions of the symmetry planes are not arbitrary. Both symmetry planes coincide with the plane contained the sphere centers, MXZ. Each individual wake oscillates in the direction parallel to the symmetric plane, generating the plane symmetric hairpin vortices, e.g. A and C.

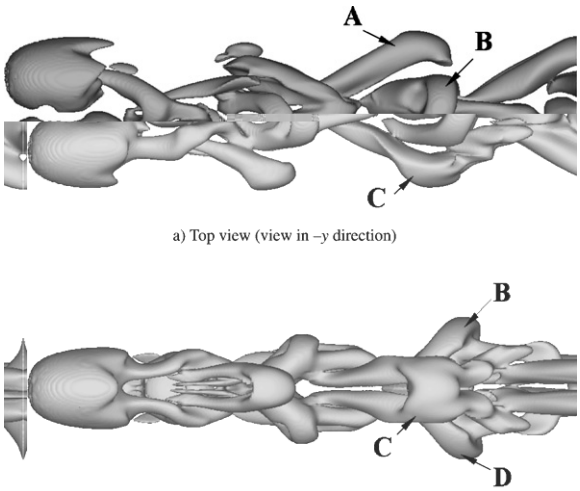

Fig. 9. Vortical structure at $Re = 300$ for $h = 1.5D$.

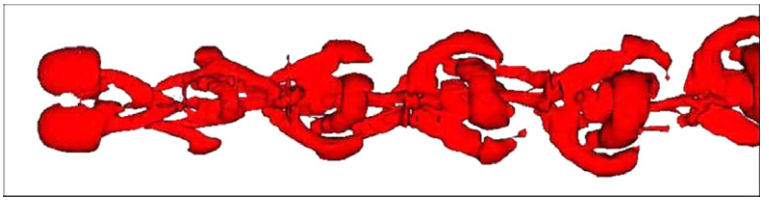

Fig. 10. Vortical structure at $Re = 300$ for $h = 1.5D$ [29].

Table 4
Comparison on the Strouhal number at $Re = 300$

	St/St_0	St_0
Schouveiler et al. [29]	0.836	0.136
Present	0.866	0.1294

St_0 is the Strouhal number for a single non-interactive sphere.

In the downstream, due to the interaction of the two wakes, the hairpin vortices out of the symmetric plane, e.g. B and D, are formed. These formations of vortical structure can be compared with that in the DNS simulation in Fig. 10. It is also found that the direction of the lateral force exerted on each sphere is almost aligned with the line connected with the centers of the spheres and there exist a proximately 180° phase shift between the drag force, as reported in [29].

The oscillation of the weak is always measured by the Strouhal number:

$$St = \frac{f_v D}{U} \tag{34}$$

where the f_v is the shedding frequency of the wake. The quantitative comparisons are summarized in Table 4.

3.3. Spherical shell in a square duct flow

This model is an initial and basic step for further simulation of cell deformations in flow. The schematic is shown in Fig. 11. In this model, thin-walled structure is involved. Either 2D shell elements [30] or 3D high-order p-elements [31] are the choices to simulate the thin-walled structures. Unlike the 2D shell elements, which need many extra efforts to avoid various kinds of locking, 3D p-elements avoid locking by choosing sufficient high-order polynomials in lateral directions. Linear or quadratic polynomials in the transversal direction are generally sufficient [33]. Furthermore, if the Gauss–Lobatto interpolation points are selected, then the high-order accurate approximation and better convergent rate can be achieved, and the higher-order

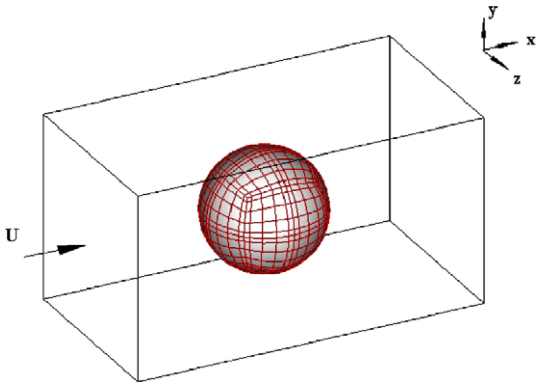

Fig. 11. A spherical shell in a duct flow.

polynomial oscillations on the boundary observed in case of the evenly distributed interpolation points [32] can be suppressed. Another advantage is that no rotational DOF is required, which makes it convenient for the geometrical nonlinear analysis. In our computation, we choose 5–6 order polynomials in the lateral direction and quadratic order in the transversal direction. Before carrying out the fluid–structure simulation, we first perform the element test on the problem known as *pinched hemisphere with* 18° *hole*.

As shown in Fig. 12 , two inward and two outward forces are imposed on a hemisphere with an 18° hole at the top. Only one quarter of the hemisphere is taken into computation because of the symmetry conditions.

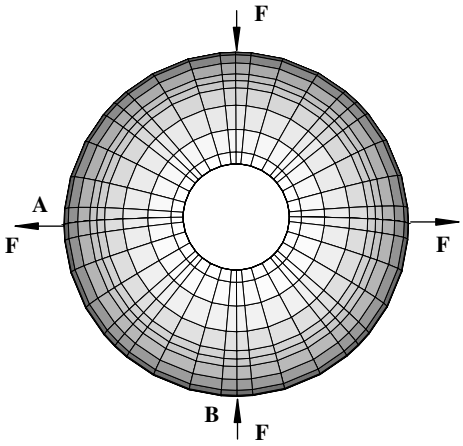

Fig. 12. Mesh1 and load configuration.

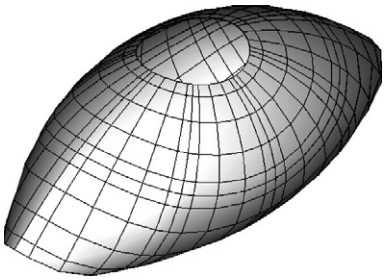

Fig. 13. Deformation at $F = 200$ (mesh1).

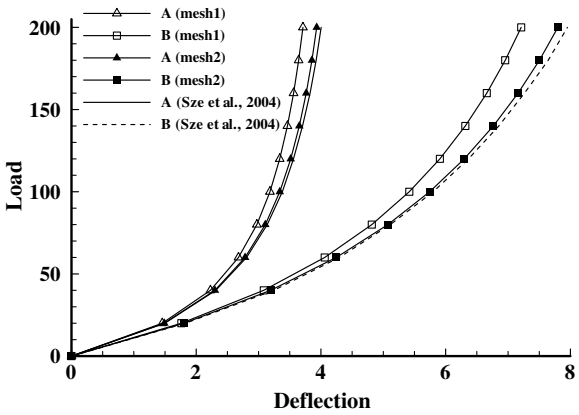

Fig. 14. Load–deflection curve comparison.

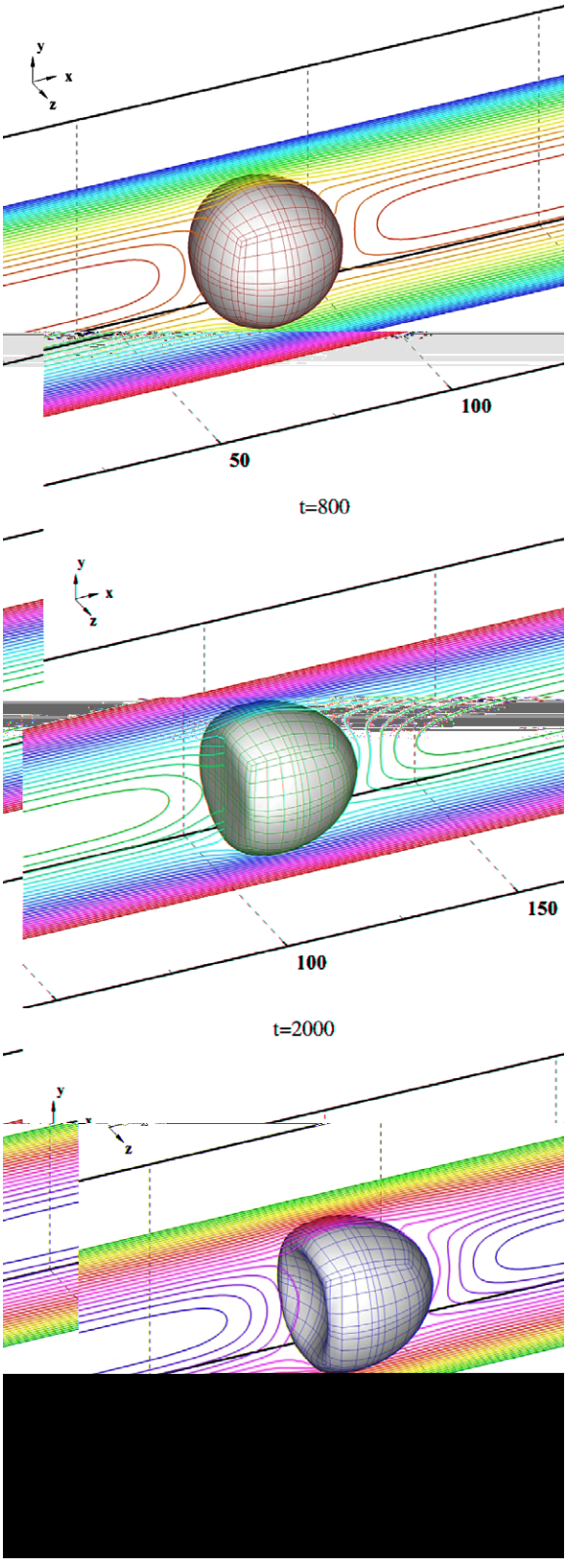

Fig. 15. Spherical shell deformations at different time.

The radius is 10 and the thickness is 0.04. The material properties are $E = 6.825 \times 10^7$ and $v = 0.3$. Two meshes are use for comparison: mesh1 discretizes the quarter hemisphere into four $6 \times 6 \times 3$-node elements and mesh2 into four $7 \times 7 \times 3$-node elements.

Our results on the deformation of the hemisphere are compared to those from [34] in Fig. 14, where the corresponding value of load they used in the figures is the sum of the magnitudes at A and B, being the double of F in our computation. The final deformation of the hemisphere at the maximum load, $F = 200$, is shown in Fig. 13. The finer mesh, mesh2, provides more accurate results that agree better with the previous results. However, from Figs. 13 and 14, mesh1 is good enough for qualitative study, and it is computationally more economical than mesh2. We decide to employ-node element in the following example, which is mainly for the qualitative investigation.

Now we turn to the simulation of spherical shell deformation in the duct flow. The size of fluid domain is $260 \times 48 \times 48$ with respect to the x–y–z directions. The radius of the spherical shell is 15 and the thickness is 0.3. The spherical shell is discretized into 24 $6 \times 6 \times 3$-node elements and the initial position of the center point is placed at $(70, 16, 16)$. The relaxation time, the streamwise pressure gradient and the fluid mass density are given as 0.97, 3.5×10^{-5}, 1.0, respectively. The solid has the same mass density as the fluid, and the material is the neo-Hookean material with the same strain energy density per unit in Eq. (26). The material parameters are $\mu = 0.1$ and $\lambda = 10.0$. The flow starts from stationary state with all the velocities being zero.

The deformations of the shell and the slices of the streamwise velocity contours on the MXY plane at different times are illustrated in Fig. 15. In the straight duct flow, the streamwise velocity component is dominant compared to those in the other two directions. It is obvious that the streamwise fluid velocities decrease from the channel center to the wall. Such fluid velocity field causes the similar velocity distribution on the solid shell. The streamwise velocity difference in the spanwise direction on the shell makes the parts near the central line move faster than the parts relatively farther from the central line. So it can be found that the upwinding part of the shell in the flow direction becomes more and more flat, and then turns concave. As the flow evolves, the locations of the mesh grids in Fig. 15 indicate that the material points on the spherical shell are rolled over in the concave. This deformation tendency is qualitatively similar to that in the cylindrical pipe in [35]. As demonstrated in [35], the mechanism of the deformation often causes the physical instability of the shell, and in some cases, the shell will never reach a steady state.

It is also found that, although the high-order element has the advantages mentioned earlier, it raises the condition number of stiffness matrix, which reduces the convergence rate, especially when the upwinding part of the shell is very flat in our numerical experiment.

4. Conclusion

In this paper, the lattice Boltzmann method is extended to solve the 3D fluid/elastic-body interaction problems by introducing the Lagrange multiplier and solid governing equations, and is successful in the test problems. In the developed LBM–DLM/FD method, the mesh for fluid flow is the fixed Eulerian mesh that avoids the re-meshing procedure and has the capacity to deal with complex geometry. The mesh for solid motion is a Lagrangian mesh so that the conventional schemes for the solution of solid deformation can be incorporated easily. The method reserves the advantages of LBM and DLM/FD.

Some numerical experiments are conducted in the paper. On one hand, these experiments verify the algorithm and illustrate the capability of the method to solve the fluid/elastic–structure problems and problems with complex geometry. On the other hand, these experiments give the first step for further exploration of more complicated problems.

References

[1] S.A. Berger, L.-D. Jou, Flows in stenotic vessels, Annu. Rev. Fluid Mech. 32 (2000) 347.
[2] J. De Hart, G.W.M. Peters, P.J.G. Schreurs, F.P.T. Baaijens, A three-dimensional computational analysis of fluid–structure interaction in the aortic valve, J. Biomech. 36 (2003) 103.
[3] Krzysztof Boryczko, Witold Dzwinel, David A. Yuen, Dynamical clustering of red blood cells in capillary vessels, J. Mol. Model 9 (2003) 16.

[4] N.A. N'Dri, W. Shyy, R. Tran-Son-Tay, Computational modeling of cell adhesion and movement using a continuum-kinetics approach, Biophys. J. 85 (2003) 2273.
[5] J. Donea, S. Giuliani, J.P. Halleux, An arbitrary Lagrangian–Eulerian finite element method for transient dynamic fluid–structure interactions, Comput. Meth. Appl. Mech. Eng. 33 (1982) 689.
[6] C.S. Peskin, Numerical analysis of blood flow in the heart, J. Comput. Phys. 25 (1977) 220.
[7] Lucy Zhang, Axel Gerstenberger, Xiaodong Wang, Wing Kam Liu, Immersed finite element method, Comput. Methods Appl. Mech. Eng. 193 (2004) 2051.
[8] R. Glowinski, T. Pan, J. Périaux, A fictitious domain method for external incompressible viscous flow modeled by Navier–Stokes equations, Comput. Meth. Appl. Mech. Eng. 112 (1994) 133.
[9] Z. Yu, N. Phan-Thien, R.I. Tanner, Dynamic simulation of sphere motion in a vertical tube, J. Fluid Mech. 518 (2004) 61.
[10] F.P.T. Baaijens, A fictitious domain/mortar element method for fluid–structure interaction, Int. J .Numer. Meth. Fluids 35 (2001) 743.
[11] Z. Yu, A DLM/FD method for fluid/flexible-body interactions, J. Comput. Phys. 207 (2005) 1.
[12] S. Chen, G.D. Doolen, Lattice Boltzmann method for fluid flows, Annu. Rev. Fluid Mech. 30 (1998) 329.
[13] R.R. Nourgaliev, T.N. Dinh, T.G. Theofanous, D. Joseph, The lattice Boltzmann equation method: theoretical interpretation, numerics and implications, Int. J. Multiphase Flow 29 (2003) 117.
[14] A.J.C. Ladd, Numerical simulation of particulate suspensions via a discretized Boltzmann equation, Part 1.Theoretical foundation, J. Fluid Mech. 271 (1994) 285.
[15] M. Krafczyk, J. Tölke, E. Rank, M. Schulz, Two-dimensional simulation of fluid–structure interaction using lattice-Boltzmann methods, Comput. Struct. 79 (2001) 2031.
[16] D. Qi, C.K. Aidun, A new method for analysis of the fluid interaction with a deformable membrane, J. Stat. Phys. 90 (1998) 145.
[17] D. Qi, Direct simulations of flexible cylindrical fiber suspensions in finite Reynolds number flows, J. Chem. Phys. 125 (2006) 114901.
[18] Zhi-Gang Feng, Efstathios E. Michaelides, Proteus: a direct forcing method in the simulations of particulate flows, J. Comput. Phys. 202 (2005) 20.
[19] Xing Shi, Nhan Phan-Thien, Distributed Lagrange multiplier/fictitious domain method in the framework of lattice Boltzmann method for fluid–structure interactions, J. Comput. Phys. 206 (2005) 81.
[20] T. Lee, C. Lin, Pressure evolution lattice-Boltzmann-equation method for two-phase flow with phase change, Phys. Rev. E 67 (2003) 056703.
[21] D. Kandhai, A. Koponen, A. Hoekstra, M. Kataja, J. Timonen, P.M.A. Sloot, Implementation aspects of 3D lattice-BGK:boundaries, accuracy, and a new fast relaxation method, J. Comput. Phys. 150 (1999) 482.
[22] Y. Qian, D. d'Humières, P. Lallemand, Lattice BGK models for Navier–Stokes equation, Europhys. Lett. 17 (1992) 479.
[23] C.K. Aidun, Y. Lu, E. Ding, Direct analysis of particulate suspensions with inertia using the discrete Boltzmann equation, J. Fluid Mech. 373 (1998) 287.
[24] Ted Belytschko, Wing Kam Liu, Brian Moran, Nonlinear Finite Elements for Continua and Structures, Wiley, 2000.
[25] T. Sussman, K.J. Bathe, A finite element formulation for nonlinear incompressible elastic and inelastic analysis, Comput. Struct. 26 (1987) 357.
[26] I. Kim, S. Elgobashi, W.A. Sirignano, Three-dimensional flow over two spheres placed side by side, J. Fluid Mech. 246 (1993) 465.
[27] T. Tsuji, R. Narutomi, T. Yokomine, S. Ebara, A. Shimizu, Unsteady three-dimensional simulation of interactions between flow and two particles, Int. J. Multiphase Flow 29 (2003) 1431.
[28] J. Jeong, F. Hussain, On the identification of a vortex, J. Fluid Mech. 285 (1995) 69.
[29] L. Schouveiler, A. Brydon, T. Leweke, M.C. Thompson, Interactions of the wakes of two spheres placed side by side, Eur. J. Mech. B 23 (2004) 137.
[30] Henry T.Y. Yang, S. Saigal, A. Masud, R.K. Kapania, A survey of recent shell finite elements, Int. J. Numer. Meth. Eng. 47 (2000) 101.
[31] A. Düster, H. Broker, E. Rank, The *p*-version of the finite element method for three-dimensional curved thin walled structures, Int. J. Numer. Meth. Eng. 52 (2002) 673.
[32] Jan Mandel, Iterative methods for *p*-version finite elements: preconditioning thin solids, Comput. Methods Appl. Mech. Eng. 133 (1996) 247.
[33] Y. Basar, U. Hanskotter, Ch. Schwab, A general high-order finite element formulation for shells at large strains and finite rotations, Int. J. Numer. Meth. Eng. 57 (2003) 2147.
[34] K.Y. Sze, S.-J. Zheng, S.H. Lo, A stabilized eighteen-node solid element for hyperelastic analysis of shells, Finite Elements Anal. Des. 40 (2004) 319.
[35] Christophe Quéguiner, Dominique Barthès-Biesel, Axisymmetric motion of capsules through cylindrical channels, J. Fluid Mech. 348 (1997) 349.